scientific reports



OPEN

Tailoring the performance of DLC coatings through interlayer engineering

Mohsen Samiee, Mohamad Javad Eshraghi[™] & Keivan Asadian

Diamond-like carbon (DLC) coatings have been widely studied for their exceptional hardness, low friction, and excellent wear and corrosion resistance, making them highly attractive for biomedical and industrial applications. However, their practical implementation is often hindered by internal stress and poor adhesion to metallic substrates. In this study, the effect of interlayers including plasma nitriding (PN), zirconium nitride (ZrN), and tantalum nitride (TaN) on the microstructure, wear behavior, and corrosion resistance of DLC coatings was investigated. FESEM images revealed a high density and uniformity of the DLC coatings in all three samples, with crack-free and pore-free surfaces. AFM analysis indicated that the ZrN+DLC and TaN+DLC samples, with surface roughness values of 3.42 nm and 3.31 nm respectively, exhibited smoother surfaces compared to the PN+DLC sample, which had a roughness of 42.34 nm. Wear testing showed that the TaN+DLC sample exhibited the lowest weight loss (8 mg) and wear rate (0.001901 mm³/N·m). Moreover, impedance curves indicated the highest corrosion resistance in the TaN+DLC sample. These findings demonstrate that the incorporation of ZrN and TaN interlayers significantly enhances the surface characteristics, particularly surface roughness and structural uniformity, along with the wear and corrosion resistance of DLC coatings.

Keywords DLC, SS420, PECVD, Wear, Corrosion

Surface engineering plays a crucial role in enhancing the properties of materials and extending their service life. This field is of significant interest across various industries, particularly in healthcare, dentistry, and laboratory settings. Medical and laboratory instruments, due to their constant exposure to corrosive environments and sterilization processes, are prone to surface damage and degradation. The presence of surface defects can lead to contamination buildup and compromised safety. In this regard, the application of advanced coatings presents a promising solution to address these challenges^{1,2}.

Diamond-like carbon (DLC) coatings are considered one of the most prominent surface engineering technologies. These coatings are widely used in surgical instruments, medical implants, and sensitive equipment due to their unique combination of properties such as high hardness, low friction, wear and corrosion resistance, and biocompatibility^{3–5}.

The advantages of DLC coatings include improved mechanical performance, enhanced durability of equipment, and a reduced risk of microbial contamination. Moreover, the exceptional properties of these coatings contribute to lowering maintenance and replacement costs for tools in critical industries. Ongoing scientific research continues to focus on optimizing deposition methods and enhancing the final properties of DLC coatings to expand their range of applications^{6,7}.

One of the key challenges in utilizing DLC coatings is minimizing internal stresses and improving the adhesion between the coating layer and the substrate. Selecting an appropriate interlayer can not only reduce internal stresses and enhance adhesion but also improve surface roughness and create a more uniform surface. This is particularly crucial for applications requiring high wear resistance and low friction. Microscopic analyses have demonstrated that applying a suitable interlayer reduces surface roughness and promotes better stress distribution^{8–11}.

One of the widely used methods for producing DLC coatings is plasma-enhanced chemical vapor deposition (PECVD). This technique encompasses various approaches, including radio frequency deposition, glow discharge, and pulsed direct current systems. PECVD, owing to its lower temperature compared to conventional methods such as CVD, enables the fabrication of thin films with unique physical and mechanical properties. Additional advantages of this method include plasma-based surface cleaning, the formation of high-hardness

Department of Semiconductors, Materials and Energy Research Center, Karaj, Iran. [™]email: m.eshraqhi@merc.ac.ir

layers, and excellent chemical and mechanical resistance, making it an ideal choice for diverse industrial applications 12-16.

A study revealed that the Cr_3C_2 -NiCr interlayer acts as a bonding bridge between the hard, wear-resistant DLC layer and the substrate, playing a crucial role in enhancing the overall performance of the coating. By forming a strong metallurgical bond between the two layers, this interlayer significantly improves adhesion and prevents common issues such as peeling and delamination¹⁷. Zhao et al. demonstrated that multilayer DLC/CrN coatings exhibit higher corrosion resistance compared to single-layer DLC coatings. This improvement is attributed to the formation of a layered structure that prevents the penetration of corrosive ions and creates a protective barrier within the multilayer coatings, safeguarding the underlying metal¹⁸. Another study found that a tantalum interlayer notably reduces the wear rate of DLC coatings by creating wear-resistant layers, reducing surface roughness, improving adhesion, and increasing the sp³ bond content in the DLC layer¹⁹.

Recent studies have shown that employing surface modification techniques such as plasma nitriding prior to DLC deposition can significantly enhance adhesion, reduce residual stress, and improve tribological performance. For instance, Kasiorowski et al.²⁰ and Shioga et al.²¹ demonstrated that plasma-nitrided interlayers improved the microstructure and wear resistance of DLC coatings on steel substrates.

The selection of ZrN and TaN as interlayers is based on their outstanding mechanical and chemical properties. ZrN offers high hardness, good corrosion resistance, and excellent thermal stability, which provide a robust foundation for DLC deposition. Similarly, TaN has emerged as a promising interlayer material due to its high density, excellent wear resistance, and chemical inertness. Recent studies have shown that TaN coatings can significantly improve adhesion and reduce stress in multilayer systems, particularly when deposited using RF magnetron sputtering techniques^{22,23}. The use of DLC as the top layer is attributed to its exceptional tribological and protective properties, including low friction, high wear resistance, and biocompatibility, making it an ideal candidate for medical and industrial applications²⁴.

Previous studies have utilized various interlayers to enhance the properties of DLC coatings on steel substrates. In this research, with the aim of improving DLC coating properties and expanding knowledge in this field, interlayers such as zirconium nitride (ZrN), tantalum nitride (TaN), and plasma nitriding have been employed as intermediate layers.

Materials and methods Sample preparation and coating process

In this research, AISI 420 stainless steel was selected as the substrate due to its extensive usage in medical devices. The samples, measuring $20 \text{ mm} \times 20 \text{ mm} \times 20 \text{ mm}$, were prepared through laser cutting.

Initially, the samples were ground with SiC abrasive papers up to grit size 2500 and then polished for 20 min using a 0.1 μ m diamond paste. Based on the polishing process, the surface roughness of the samples after polishing was estimated to be in the range of 2–5 nm, which is consistent with typical values for mirror-polished stainless-steel surfaces. To improve the adhesion of DLC coatings, plasma nitriding was performed on some samples for 240 min at a power of 5 kW and a voltage ranging from 500 V to 600 V. The gas mixture employed contained 75% nitrogen and 25% hydrogen by volume. A number of other samples were coated using an RF magnetron sputtering system with a 99.999% pure Zr target for 60 min, under a base pressure of 2.8×10^{-3} mbar and a power of 185 W, with a gas mixture of 10% N₂ and 30% Ar. Other samples were deposited with a 99.999% pure Ta target for 60 min, under a base pressure of 1.1×10^{-4} mbar and a power of 100 W at a temperature of 350 °C, using a gas composition of 10% N₂ and 30% Ar. In the final step, the plasma-nitrided, ZrN-coated, and TaN-coated samples were coated under 100% pure acetylene gas, at a pressure of 45 mTorr, a power of 120 W, and a deposition time of 45 min to form DLC layers using Plasma-enhanced chemical vapor deposition (PECVD).

Surface and structural characterization

Raman spectroscopy was performed using a Thermo Scientific DXR Raman microscope (USA), equipped with a DPSS: Nd: YAG continuous wave laser (wavelength = 512 nm, power = 10–90 mW, resolution = 6 cm⁻¹), to determine the types and quantities of carbon bonds in the coatings. Surface topography and roughness were analyzed using Atomic Force Microscopy (AFM), model Dimension Icon by Bruker, USA. Cross-sectional morphology and microstructure of the coatings were examined using Field Emission Scanning Electron Microscopy (FESEM), model MIRA3 by TESCAN, Czech Republic. Additionally, worn surfaces were analyzed using Scanning Electron Microscopy (SEM), model VEGA3 by TESCAN, Czech Republic, to study wear mechanisms after tribological testing.

Tribological evaluation

Wear

The wear tests were performed in accordance with ASTM G99 using a pin-on-disk apparatus. The test parameters included a Linear velocity of $0.1\,$ m/s, a sliding distance of $150\,$ m, an applied force of $2\,$ N, and a wear track diameter of $10\,$ mm. An alumina ball with a 4 mm diameter was used as the counter-body. Samples were weighed before and after the test using a high-precision digital scale to determine the weight loss. The worn surfaces were further analyzed using scanning electron microscopy (SEM-VEGA3 by TESCAN) to investigate the wear mechanisms. In addition, the coefficient of friction (CoF) was continuously recorded throughout the test to evaluate the frictional behavior of each sample. To better understand the contact conditions, the maximum Hertzian contact pressure was calculated. Considering the material properties of alumina and AISI 420 stainless steel, and the applied load of $2\,$ N, the effective elastic modulus was estimated to be approximately 275.3 GPa. Based on this, the contact radius was found to be around 33.7 μ m, resulting in a maximum Hertzian pressure of approximately 843 MPa during the wear test.

Corrosion

The corrosion resistance of the coatings was evaluated using electrochemical impedance spectroscopy (EIS), conducted in accordance with ASTM G106 standard. The measurements were performed at open circuit potential using a sinusoidal voltage signal with an amplitude of 10 mV over a frequency range from 10^{-2} to 10^4 Hz. A potentiostat (PAR 273 A) connected to a Lock-in amplifier (PAR 5210) was used for the analysis. All tests were conducted at room temperature in a 3.5% NaCl solution. A three-electrode electrochemical cell was employed, consisting of a saturated calomel electrode (SCE) as the reference (+242 mV vs. SHE), a platinum foil as the counter electrode, and the coated sample as the working electrode with an exposed area of 0.78 cm².

Result and discussion Structural characterization

The Raman spectra of the DLC samples are presented in Fig. 1. Typically, DLC structures exhibit two distinct peaks in the Raman region, appearing near 1340 cm⁻¹ and 1570 cm⁻¹. As reported in previous studies^{25–28}, these peaks correspond to the D and G bands, respectively. The G band, located around 1570 cm⁻¹, is associated with sp² carbon hybridization and indicates the presence of an ordered graphitic structure. In contrast, the D band, observed near 1340 cm⁻¹, corresponds to sp³ carbon hybridization and is commonly used to evaluate the degree of disorder in graphitic or diamond-like structures²⁹. Table 1 summarizes the parameters obtained from the Raman analysis. The sp³ content was estimated semi-quantitatively from the I_D/I_G intensity ratio obtained from the Raman spectra, as suggested by Ferrari and Robertson³⁰. The internal stress (σ) was calculated using the empirical correlation between the G peak position and the compressive stress, based on the following equation³¹:

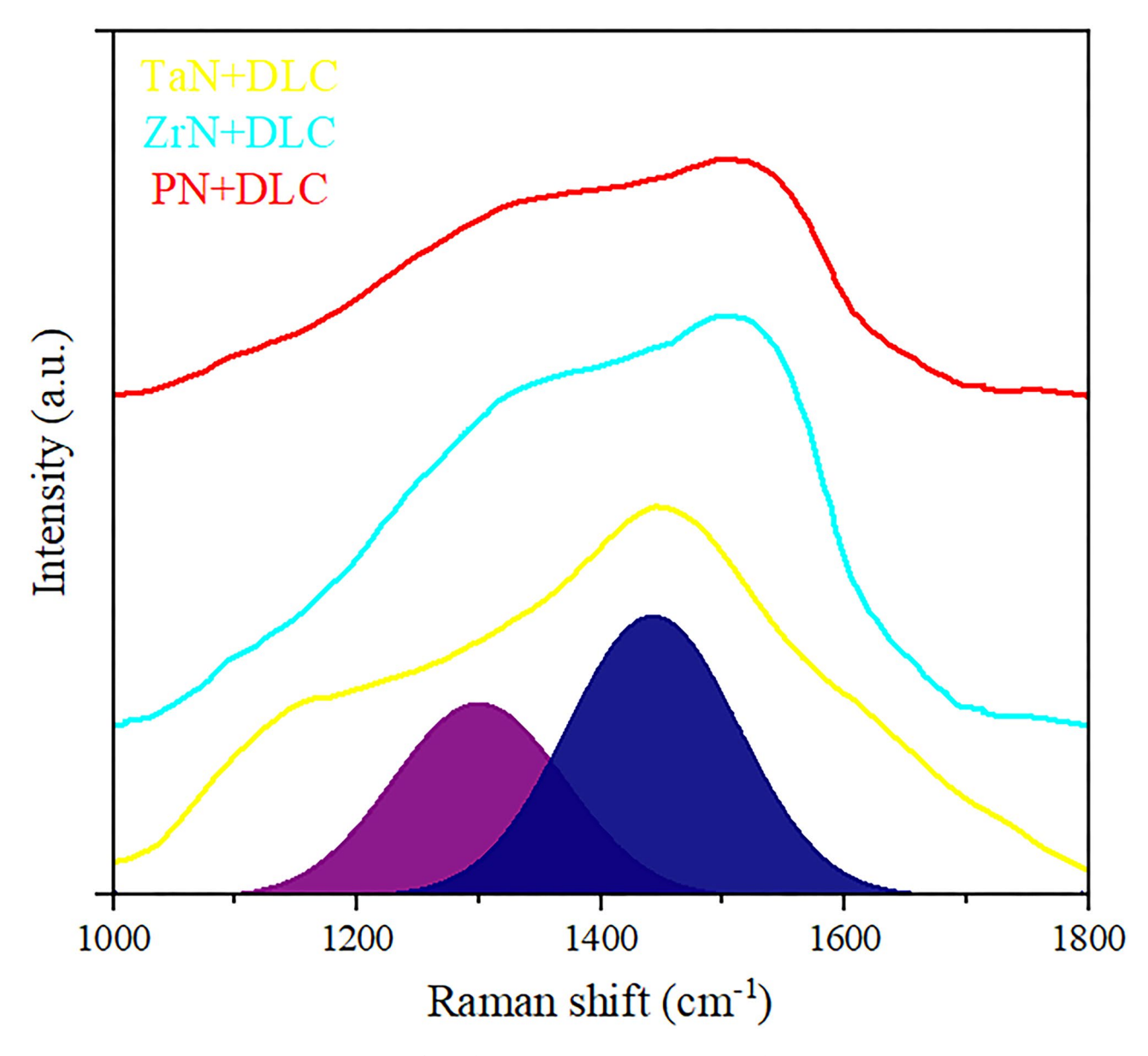


Fig. 1. Raman spectra of samples: (a) PN-DLC, (b) ZrN-DLC, and (c) TaN-DLC.

Sample	Pos. D (cm ⁻¹)	Pos. G (cm ⁻¹)	I_D/I_G	FWHM (G)	SP ³ %	σ (GPa)
PN-DLC	1346	1540	0.82 ± 0.40	170	43 ± 2	6.2
ZrN-DLC	1355	1570	0.88 ± 0.40	187	29±2	10.2
TaN-DLC	1325	1577	1.08 ± 0.51	202	20 ± 1	14.3

Table 1. Parameters extracted from the Raman analysis.

$$\sigma(\text{GPa}) = -0.0024 \times (\omega_G - 1580)$$

where ω_G is the position of the G peak in cm⁻¹. A higher shift of the G peak toward lower wavenumbers is generally indicative of higher compressive stress within the DLC structure.

Studies^{29,32,33} demonstrated that the shift of the G peak maximum toward higher Raman shifts is associated with an increase in the size of aromatic clusters within the graphitic structure, leading to elevated internal stress in DLC films. According to the data presented in Table 1, the TaN-DLC sample exhibits the highest G-band Raman shift, while the PN-DLC sample shows the lowest. Furthermore, the sp³ content and internal stress values reported in Table 1 indicate that the TaN-DLC and PN-DLC samples have the highest and lowest levels of internal stress and sp³ percentage, respectively.

The $\rm I_D/I_G$ ratio for the PN-DLC sample is 0.82 ± 0.40 , which is lower compared to the other two samples. Additionally, the ratio for the ZrN-DLC and TaN-DLC samples is 0.88 ± 0.40 and 1.08 ± 0.51 , respectively, indicating a higher degree of structural defects in the TaN-DLC sample compared to the other two. Furthermore, the full width at half maximum (FWHM) of the G-band is associated with structural defects such as changes in bond angle and bond length. According to the data in Table 1, the FWHM (G) value is higher for the TaN-DLC sample and then for the ZrN-DLC sample, compared to the PN-DLC sample. This difference suggests that the two metal nitride-containing samples have more structural defects. As previously mentioned, these defects contribute to the increase in internal stress within the structure, thus enhancing the strength of the samples. In general, the increase in internal stress reduces material deformation under external loads, consequently improving the material's durability and strength.

Figure 2 presents the cross-sectional FESEM images of DLC coatings deposited on three different interlayers: (a) plasma-nitrided (PN), (b) ZrN, and (c) TaN. The top images illustrate the overall thickness and layer configuration, while the zoomed-in images at the bottom highlight the detailed nanostructure of the DLC layers. In the PN+DLC sample (Fig. 2a), the interface between the nitrided layer and the DLC coating appears irregular and locally rough. This irregularity can be attributed to nitrogen diffusion during the plasma nitriding process, which leads to localized stress concentrations and heterogeneous nucleation. Despite this, the DLC layer is dense and free of cracks, suggesting satisfactory adhesion. In the ZrN+DLC sample (Fig. 2b), the ZrN interlayer fabricated using RF sputtering results in a flatter and denser surface. The plasma-nitrided interlayer presents localized roughness and microstructural variations due to non-uniform nitrogen diffusion, which can influence DLC nucleation. In contrast, the ZrN and TaN interlayers deposited by RF magnetron sputtering provide smoother and denser surfaces, reducing defect sites at the interface. The TaN interlayer, with its high crystallographic density, thermal stability, and chemical inertness, offers an optimal foundation for DLC growth. This smooth and defect-free interface promotes uniform nucleation and results in the TaN + DLC sample (Fig. 2c) exhibiting the most compact, continuous, and homogeneous DLC layer among the three. This is due to the dense TaN interlayer formed via magnetron sputtering at 350 °C, which provides excellent surface quality and strong bonding with the DLC layer. The interface is smooth and continuous, with no visible gaps or discontinuities. Overall, the images demonstrate that the choice of interlayer significantly affects the interface quality and coating morphology. Both ZrN and TaN interlayers, especially TaN, result in smoother and denser interfaces compared to the plasma-nitrided layer. This contributes to improved mechanical and protective performance of the final coating.

Figure 3 shows the FESEM images of the microstructure of the coated samples. In Fig. 3a, the microstructure of the DLC coating on the plasma nitrided (PN) substrate is visible. The surface of the sample appears relatively homogeneous, but small roughness and scattered islands can be detected in some areas. These irregularities may result from the initial plasma nitriding process that affected the substrate before applying the DLC coating, leading to the formation of uneven microstructures. This process alters the grain boundary morphology and induces localized stress variations, which can cause non-uniform nucleation sites during the DLC deposition, ultimately resulting in a rougher or island-like surface texture. No porosity or voids are observed in the DLC coating in this image, indicating the high quality of the PECVD coating process. This suggests that the coating is highly dense and has effectively covered the substrate surface. In Fig. 3b, the surface of the DLC coating on the zirconium nitride (ZrN) intermediate layer appears much smoother and more uniform compared to the PN-DLC sample. Similar to the previous sample, no porosity or voids are observed on the coating surface. This indicates that the DLC coating has grown continuously and defect-free on the intermediate layer surface. Since the RF sputtering process was used to create the ZrN intermediate layer, this layer has provided a very smooth and dense surface for the DLC coating. In Fig. 3c, the DLC coating on the tantalum nitride (TaN) intermediate layer covers the surface well, with no signs of porosity or voids in the coating. Similar to the ZrN-DLC sample, the surface of this sample also appears uniform, but due to differences in the properties of the TaN intermediate layer, the coating structure is slightly different. The absence of porosity and voids in this image further confirms that the DLC coating has grown well on the TaN intermediate layer. Since the magnetron sputtering process was

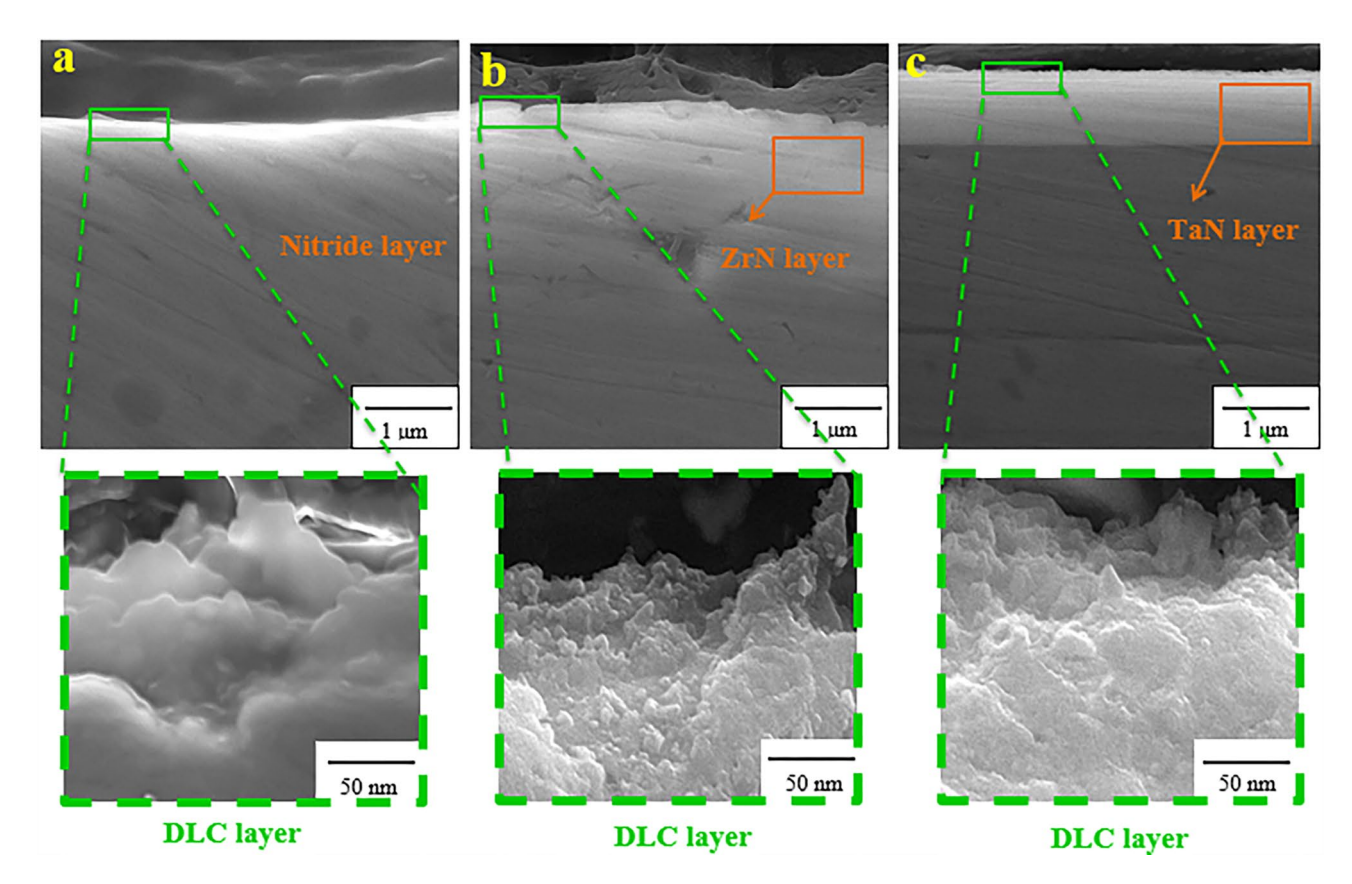


Fig. 2. FESEM images of the cross-sectional surface: (a) PN+DLC, (b) ZrN+DLC, and (c)TaN+DLC.

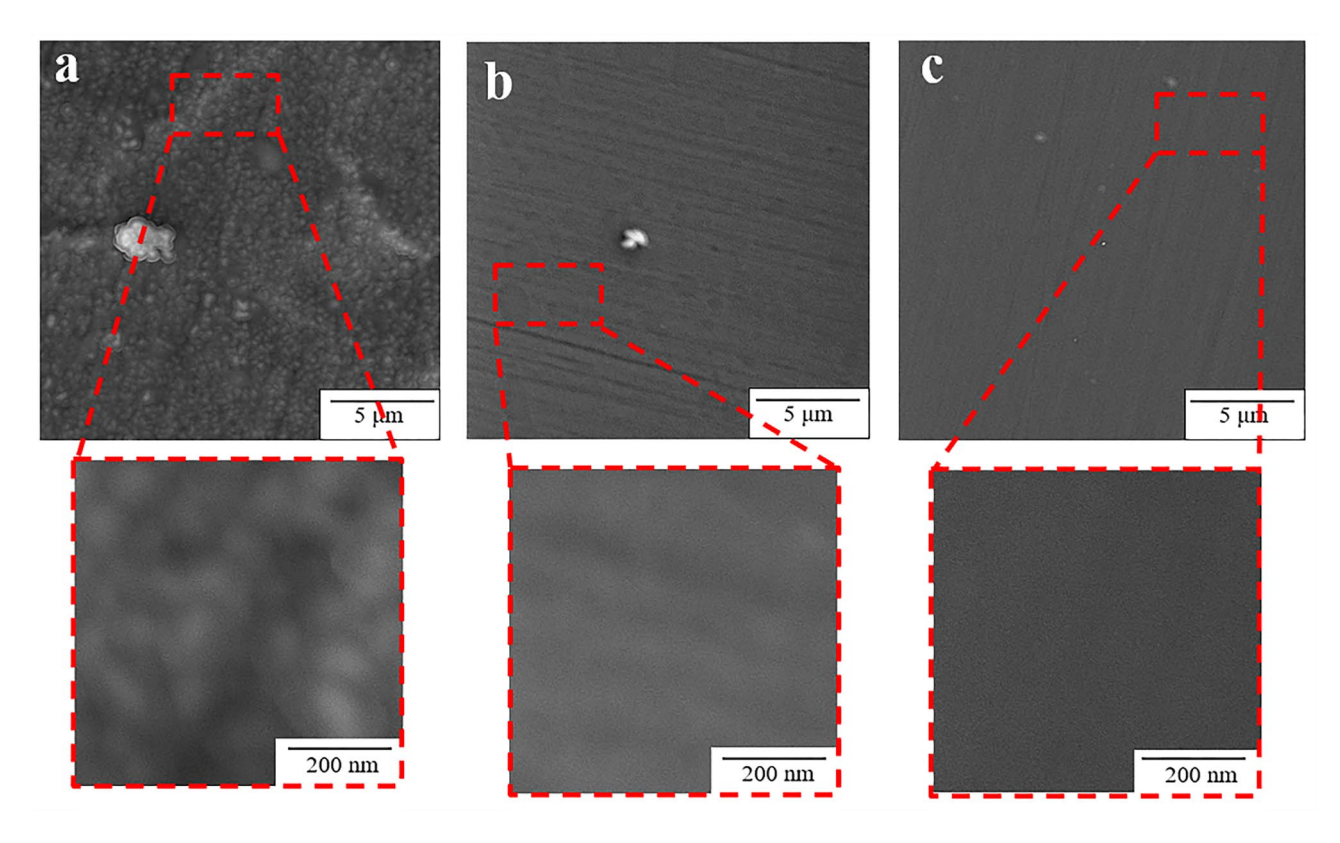


Fig. 3. FESEM images of the microstructure (a) PN + DLC, (b) ZrN + DLC, (c) TaN + DLC.

Scientific Reports |

carried out under 350 °C conditions with the appropriate gas mixture, the resulting TaN layer has high density and excellent surface quality, which directly impacts the final quality of the DLC coating.

Based on Figures a, b, and c, the surface of all three samples is uniformly coated with DLC, and no porosity or voids are observed. This can be attributed to the appropriate thickness of the DLC coating and the high quality of the PECVD coating process. Although the presence of pores in DLC coatings has been reported in the studies by Zhang et al.³⁴, in this study, the formed coatings are free of any surface defects and exhibit excellent uniformity. Additionally, based on the provided images, the DLC coatings lack grain boundaries, indicating their amorphous (non-crystalline) structure. Therefore, it can be concluded that all the coatings formed do not possess crystalline order and have an amorphous, dense structure.

Figure 4 shows the AFM images of the coated samples. In Fig. 4a, the surface of the DLC-coated sample on the plasma nitrided (PN) intermediate layer reveals a relatively coarse morphology with prominent peaks and deep valleys. This structure, resulting from the nitriding process, consists of regions with high density and a non-homogeneous distribution of surface islands. Plasma nitriding typically induces compressive stresses and leads to the growth of denser grains, with its direct effect being visible in the increase of surface roughness.

Considering the average roughness (Ra) of 42.34 nm for this sample, it is evident that the application of the DLC coating has increased the island density and strengthened the bond between the DLC layer and the substrate. On the other hand, this higher roughness is attributed to the surface heterogeneities created as a result of the nitriding process.

Figure 4b shows the surface morphology of the ZrN+DLC sample, which has an average Ra of 3.42 nm. This sample exhibits a smoother and more uniform surface compared to the PN+DLC sample, indicating the beneficial effect of the ZrN intermediate layer in reducing surface defects and achieving uniform stress distribution during the coating process. The ZrN intermediate layer, due to its high mechanical properties and wear resistance, not only provides a strong foundation for the growth of the DLC layer but also facilitates better stress distribution across the surface. These features result in a smoother and more resilient surface, offering better performance against wear and corrosion. Additionally, the smoother surface of this sample reduces surface friction, making it suitable for applications that require high-precision surfaces.

In the TaN + DLC sample (Fig. 4c), similar to the ZrN + DLC sample, the surface exhibits a relatively smooth and uniform structure. The surface roughness in this sample is 3.31 nm. This reduction in roughness compared to the ZrN + DLC sample indicates the positive effect of the TaN intermediate layer in improving surface quality and reducing structural defects. The TaN intermediate layer, due to its high thermal resistance and chemical stability, provides an ideal substrate for the growth of the DLC layer. This characteristic results in more uniform stress distribution and reduced surface heterogeneities. The dense and homogeneous structure of this sample, in comparison to the other samples, indicates higher compaction and better distribution of surface islands after the DLC coating is applied. The improved uniformity observed in the ZrN + DLC and TaN + DLC samples compared to PN + DLC can be attributed to the superior structural characteristics of the ZrN and TaN interlayers. These interlayers provide smoother and denser foundations due to the nature of the sputtering process and the resulting fine-grained microstructures. In contrast, plasma nitriding creates a rougher and less homogeneous surface, which affects the growth of the upper DLC layer and results in more pronounced irregularities. Therefore, the physical and structural properties of each interlayer play a key role in determining the uniformity of the final DLC coating.

Tribological performance

In Fig. 5, the SEM image of the worn surface of the uncoated sample is shown, while Fig. 6 shows the worn surfaces of the coated samples, and Fig. 7 illustrates the weight loss of both coated and uncoated samples. In the uncoated sample (Fig. 5), deep and continuous scratches are visible on the surface, clearly indicating severe wear resulting from the contact between the pin and the surface. The primary wear mechanism in this sample is abrasive wear, as the surface lacks any protective coating. Consequently, hard particles on the pin surface penetrate the substrate and create permanent longitudinal grooves during relative motion. The weight loss of this sample is the highest, measured at 63 mg, indicating significant material removal due to wear. Additionally, the specific wear rate is considerably higher compared to the coated samples. These findings reveal that the absence of a protective layer makes the surface highly susceptible to abrasive forces. Moreover, no mechanism is present to mitigate internal stresses or enhance surface resistance against wear, resulting in a dominant abrasive wear mechanism.

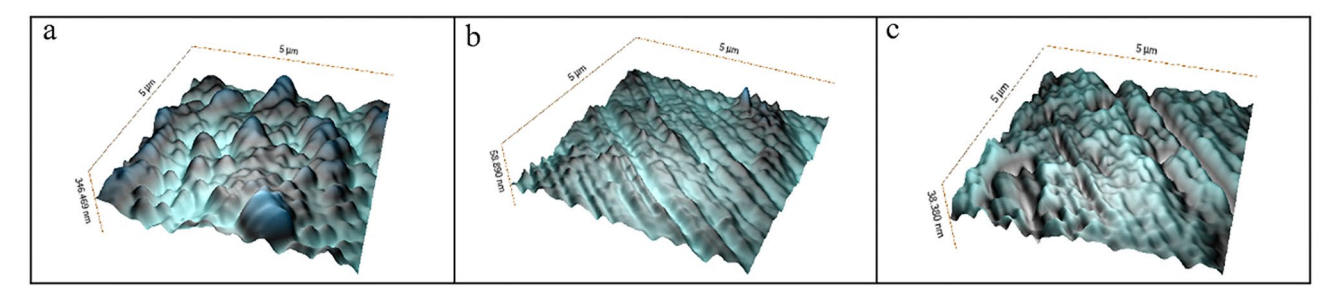


Fig. 4. AFM images of the surface morphology (a) PN+DLC, (b) ZrN+DLC, and (c) TaN+DLC.

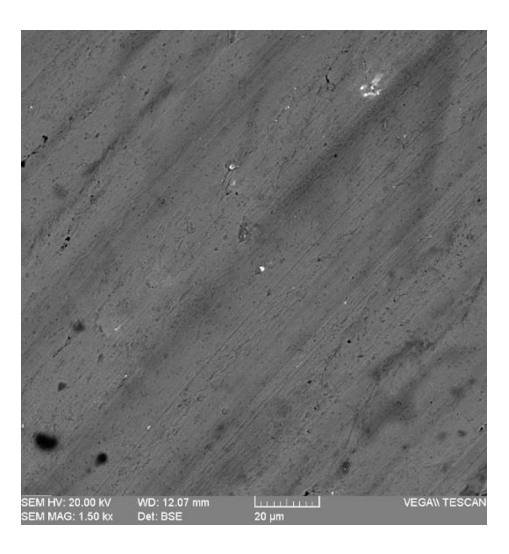


Fig. 5. SEM image of the worn surface of the uncoated sample.

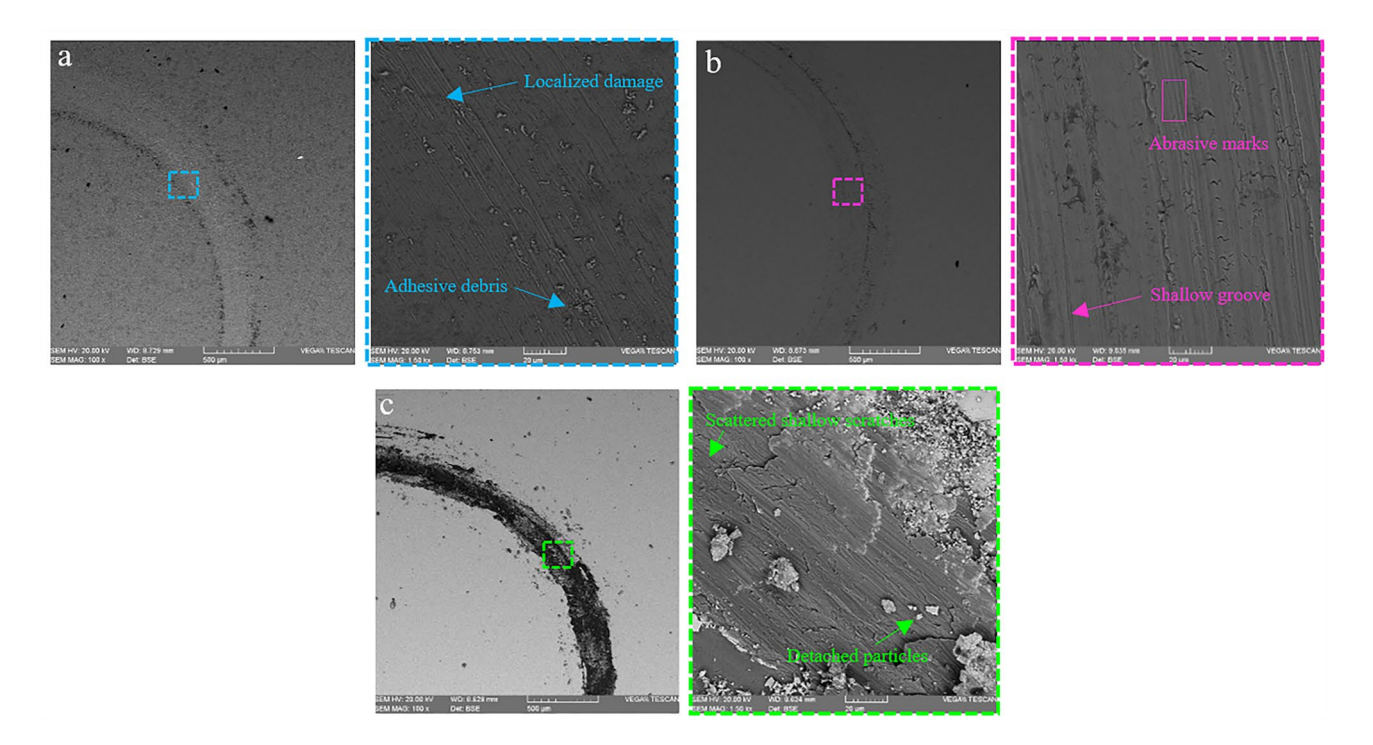


Fig. 6. SEM images of worn surfaces after tribological testing: (a) PN + DLC, showing moderate grooves and adhesive wear features; (b) ZrN + DLC, exhibiting shallower grooves and more uniform wear pattern; (c) TaN + DLC, with minimal surface damage and scattered shallow scratches, indicating superior wear resistance.

In Fig. 6a, the scratches observed are fewer and shallower compared to the uncoated sample, indicating a higher wear resistance for this sample relative to the substrate. This improvement is attributed to the application of the DLC coating over the plasma nitrided interlayer, which acts as a barrier between the pin and the substrate, preventing the formation of deep grooves. However, some noticeable and relatively defined scratches are still visible on the surface, which can be attributed to the less homogeneous structure of the plasma nitrided interlayer. The weight loss for this sample is 11 mg and its wear rate is $0.00524 \text{ mm}^3/\text{N·m}$, reflecting an intermediate performance between the uncoated sample and the ZrN+DLC-coated sample. The dominant wear mechanism in this sample is adhesive wear, arising from the relative adhesion between the DLC layer and the pin surface.

The SEM images of the ZrN+DLC sample (Fig. 6b) reveal a relatively smoother and more uniform surface compared to the uncoated and PN+DLC sample. Shallow wear tracks and fewer, more evenly spaced scratches are observed, indicating uniform stress distribution on the surface and higher wear resistance of this sample. The DLC coating on the ZrN interlayer, due to its homogeneous structure and better adhesion, has effectively

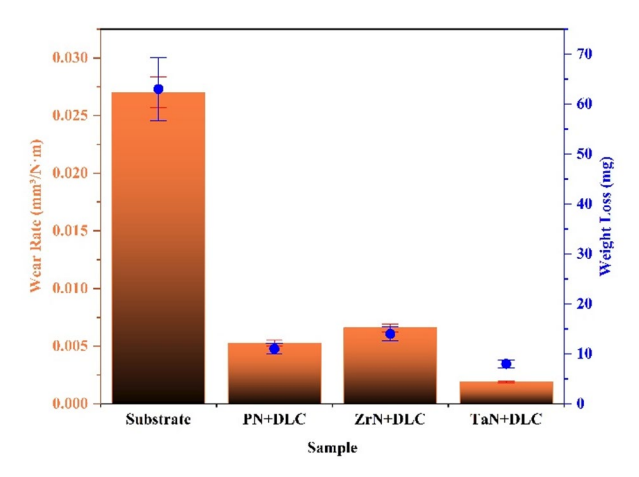


Fig. 7. Variations in Specific Wear Rate and weight loss.

reduced wear. Based on Raman data, the broader G-band width in this sample compared to PN+DLC suggests a higher presence of structural defects, contributing to improved wear resistance. The weight loss for this sample is 14 mg, and its wear rate is 0.006582 mm³/N·m, demonstrating an improvement compared to PN+DLC. The dominant wear mechanism in this sample is a combination of adhesive and mild abrasive wear, attributed to the homogeneity, smooth surface, and better adhesion of the DLC layer to the ZrN interlayer.

The figures of the TaN+DLC sample (Fig. 6c) show the least amount of scratching and wear compared to the other samples. The surface scratches are scattered and very shallow, indicating the very high wear resistance of this sample. The presence of the TaN interlayer, which was created using magnetron sputtering at 350 °C with a uniform thickness, plays a significant role in enhancing the strength and adhesion of the DLC layer. The reduction in surface roughness indicates the uniformity and homogeneity of the DLC coating. Additionally, according to Raman data, the TaN+DLC sample has the highest internal stress, contributing to its increased strength and wear resistance^{27,34,35}.

The higher $I_{\rm D}/I_{\rm G}$ ratio in this sample, among the three coated samples, indicates more structural defects in this sample. These defects, caused by high internal stress, lead to increased strength and surface resistance. The weight loss of this sample is 8 mg, and its wear rate is 0.001901 mm³/N·m, showing the best performance among all the samples. The predominant wear mechanism in this sample is mild abrasive wear with minimal adhesion, which is attributed to the high internal stress, excellent interlayer adhesion, and the uniformity of the surface.

The variation of the CoF is shown in Fig. 8. The uncoated substrate exhibits a relatively high and unstable CoF, increasing up to 0.5 due to severe abrasive interaction. In contrast, the DLC-coated samples display significantly lower and more stable friction behavior. Notably, the TaN+DLC sample demonstrates the lowest average CoF, indicating optimized frictional performance and superior wear resistance.

Corrosion resistance

Figure 9 shows the Nyquist plots (Z' versus –Z") for the examined samples. As seen, in the Nyquist plots, the frequency increases from the right side of the graph toward the left (counterclockwise). Therefore, the point at the far left of the plot represents the highest frequency, while the point at the far right represents the lowest frequency. In these plots, an increase in the diameter indicates enhanced corrosion resistance of the system. Based on the Nyquist plots, it is evident that the uncoated sample exhibits the lowest corrosion resistance, while the TaN+DLC-coated sample shows the highest corrosion resistance. Furthermore, it is clear that among the other two samples, the PN+DLC-coated sample has a smaller Nyquist semicircle diameter compared to the ZrN+DLC-coated sample.

Figure 10 shows the Bode plots of the uncoated and coated samples. In the Bode impedance modulus plots, the impedance modulus at the lowest frequency can indicate the overall corrosion resistance of the system³⁶. Therefore, based on the figure, it is evident that the uncoated sample and the TaN+DLC-coated sample exhibited the lowest and highest impedance at the lowest frequency, corresponding to the lowest and highest corrosion resistance, respectively. Additionally, the impedance at the lowest frequency for the ZrN+DLC sample was higher than that of the PN+DLC sample. Furthermore, in all the Bode impedance modulus plots, the impedance at the highest frequency indicates the solution resistance. Accordingly, in the uncoated sample, due to high corrosion rates and greater release of iron cations into the solution, the solution conductivity increased, and consequently, the solution resistance was lower compared to the other samples. On the other hand, the highest impedance at the highest frequency (and thus the highest solution resistance) was observed in the TaN+DLC-coated sample, providing further evidence of a lower concentration of iron cations resulting from corrosion reactions in the solution.

The exact resistance values of these systems should be determined by modeling the results using an electrochemical equivalent circuit. To determine the shape of the electrochemical equivalent circuit, it is essential to determine the number of time constants of the system. The number of time constants refers to the number of parallel capacitors/resistors in the equivalent circuit. By examining the Bode phase angle plots, we can determine

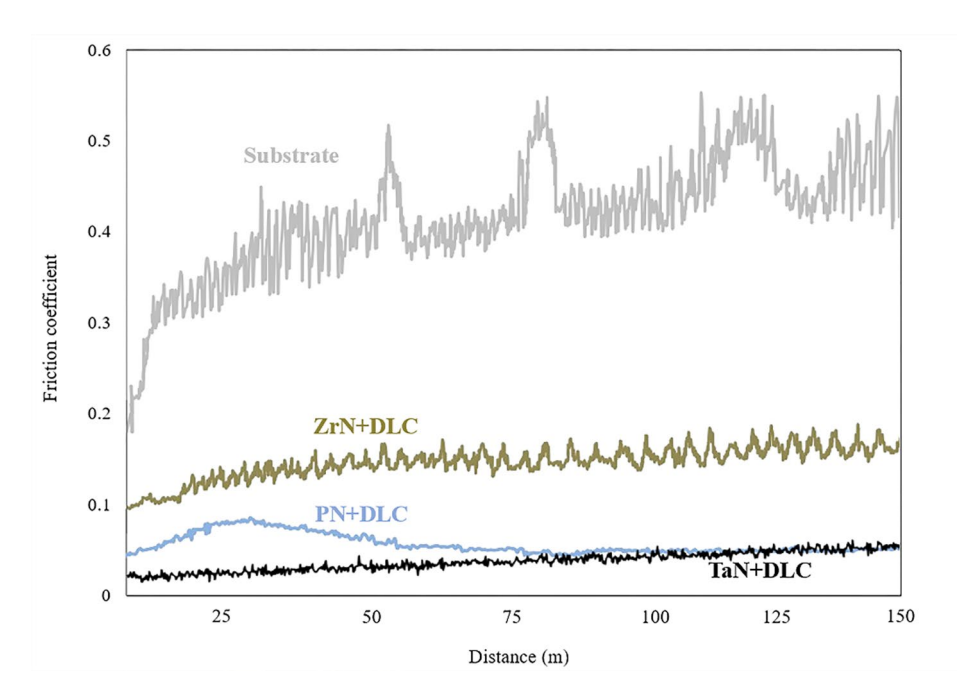


Fig. 8. Variation of CoF with distance for the uncoated substrate and DLC-coated samples.

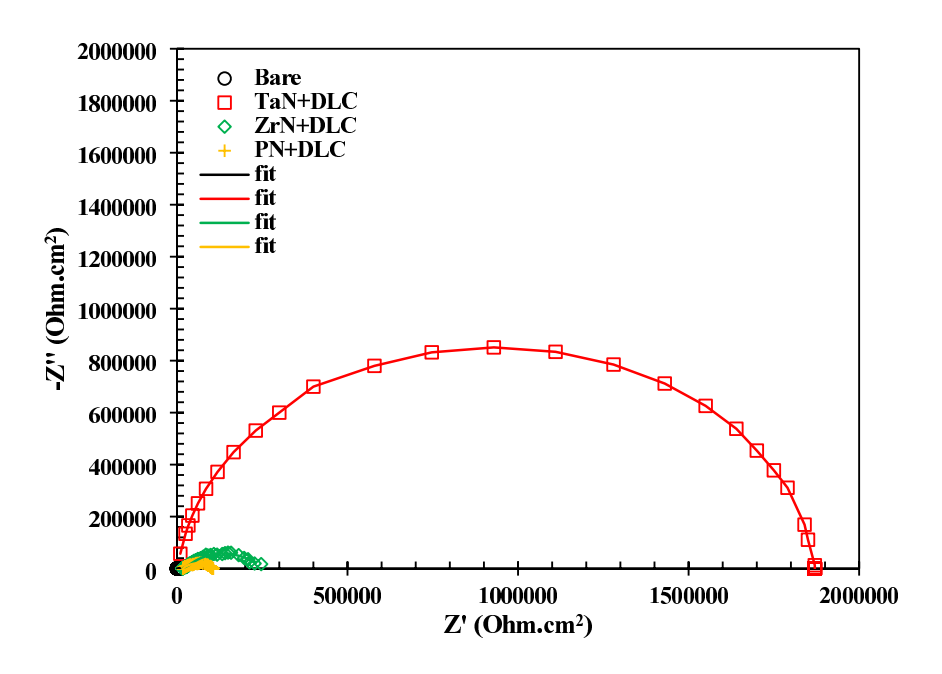


Fig. 9. Nyquist plots of the samples after immersion, along with the fitted results from the EIS test on the corresponding electrochemical equivalent circuit (points represent experimental data and lines represent the fitted results).

the number of time constants for the systems, which will aid in the determination of the electrochemical equivalent circuit. As shown in Fig. 11, some samples exhibit a single peak, while others show two overlapping peaks in their Bode phase angle plots, corresponding to single and double time constant systems, respectively. To obtain more accurate electrochemical parameters, the impedance test results were fitted to the electrochemical equivalent circuits shown in Fig. 11.

The equivalent circuit with double time constants includes three resistances (sequentially representing solution resistance, coating resistance, and charge transfer resistance) and two constant phase elements (CPEs) associated with the coating and the double layer. In the single-time-constant equivalent circuit, only elements related to the coating are visible due to the inability of the electrolyte to penetrate the coating and reach the

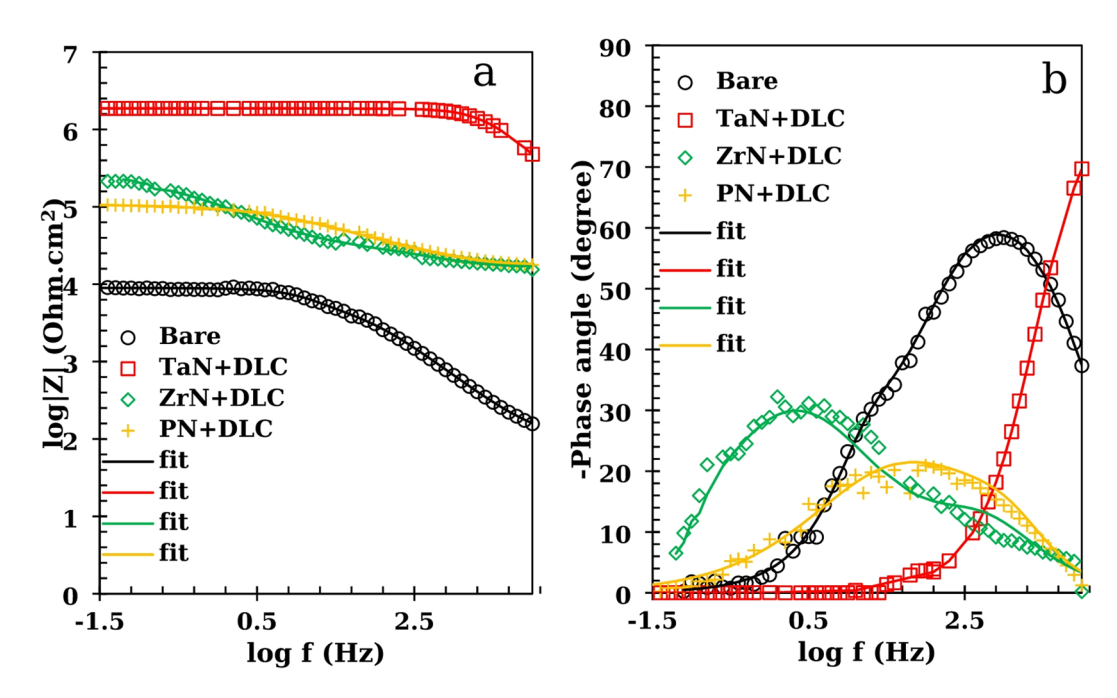


Fig. 10. (a) Bode impedance and (b) Bode phase angle plots of uncoated and coated samples after immersion in a saline solution (experimental data points and fitted results are represented by the data points and fitting lines, respectively).

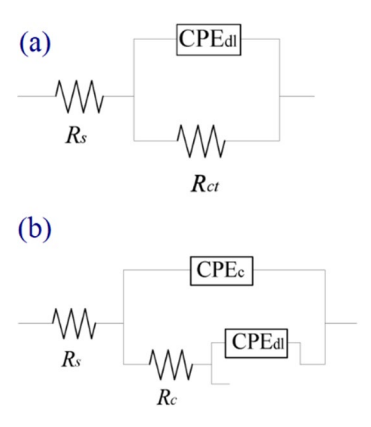


Fig. 11. Equivalent circuits of (a) single time constant and (b) double time constant.

metal surface; only the TaN + DLC sample corresponds to this circuit. In these equivalent circuits, constant phase elements (CPEs) are used instead of ideal capacitors due to the non-parallel nature of the double-layer planes formed between the electrode surface and the electrolyte, as well as the surface roughness of the electrode and coating. The distinction between these two elements is apparent in their respective impedance expressions. The impedance of a capacitor is given by $Z = \frac{1}{j\omega} \frac{1}{C}$, and for CPE, it is expressed as $Z = (\frac{1}{(Y0j\omega)})^{n37}$. In these formulas,

C represents capacitance, ω is the angular frequency, Y_0 is admittance (the inverse of impedance and equivalent to the capacitance parameter in an ideal capacitor), and j is the imaginary unit, $\sqrt{-1}$. As can be seen, the difference between these two lies only in the exponent n, which is a numerical value between zero and one. The value of zero represents an ideal resistor, and the value of one represents an ideal capacitor³⁸. The modeling of the measured samples with the electrochemical equivalent circuit was performed using the ZsimpWin software, and the results are shown in Figs. 9 and 10. As can be observed, the modeling has successfully matched the Nyquist and Bode plots, indicating the reliability of the results obtained from the modeling. The values of the parameters obtained from this modeling are reported in Table 2.

In Table 2, the values of the equivalent capacitance of the coating and the double layer were calculated using Eqs. (1) and $(2)^{39}$.

$$C_c = (Y0_c \times R_c^1 - n)^{1/n} \tag{1}$$

Sample	R _s (ohm.cm ²)	Y0 (μS.sec ⁿ .cm ⁻²)	n ₁	R _c (ohm.cm ²)	C _C (µF/cm ²)	Y0 _{dl} (μS.sec ⁿ .cm ⁻²)	n ₂	R _{ct} (ohm.cm ²)	C _{ct} (μF/cm ²)
Substrate	134.23	20.21	0.79	5993	101.18	40.95	1	2872	41.01
PN+DLC	18,820	0.014	1	8335	0.0440	1.26	0.55	80,820	1.522
ZrN+DLC	16,630	0.080	0.77	13,960	0.0311	0.713	0.61	216,200	0.568
TaN + DLC	8371	0.002	0.94	5,603,000	0.005	-	-	-	-

Table 2. Results of the impedance test modeling on the electrochemical equivalent circuit.

$$C_{ct} = (Y0_{ct})^{1/n} \times ((R_{ct} \times R_s)/(R_{ct} + R_s))^{(1/n)n}$$
(2)

According to Table 2, it is clear that with surface coating, the values of coating resistance and charge transfer resistance have significantly increased compared to the uncoated sample. Additionally, the reduction in solution resistance upon applying the coating indicates a decrease in the corrosion rate of the coated samples. Moreover, it is evident that the sum of the charge transfer resistance and coating resistance in the TaN+DLC sample is significantly higher than in the other samples, indicating a greater corrosion resistance for this sample. The absence of the second time constant in this sample is due to the inability of the electrolyte to reach the metal surface. In fact, the only interface between this sample and the electrolyte is the coating surface, whereas in the other coated samples, due to the electrolyte passing through the coating, there are two interfaces between the sample and the electrolyte: one between the coating and the electrolyte, and the other between the metal surface and the electrolyte. The lower equivalent capacitance of the coating is also further evidence of the electrolyte's inability to penetrate the coating and the higher corrosion resistance in this sample. It has been shown that the crystalline structure of TaN is completely stable and well-organized, and this structural density leads to strong bonding between tantalum and nitrogen atoms, resulting in excellent resistance to the penetration of corrosive agents into the coating 40,41.

Additionally, when the TaN-coated sample is placed in a corrosive environment, a very thin, resistant, and passive layer of tantalum oxide (Ta₂O₅) forms on the electrode surface, preventing direct contact with the electrode. Furthermore, since TaN has a low surface free energy, it has little thermodynamic tendency to react with other materials, thus exhibiting high corrosion resistance. Moreover, TaN possesses suitable electrochemical properties that place its electrode potential within the passive range, ensuring that this coating remains passive in a saline corrosive environment and is resistant to corrosion 42,43. Following this, the ZrN + DLC-coated sample exhibited higher anti-corrosion properties than the other samples. This coating, due to its high density and low porosity, creates effective barrier properties against electrolyte penetration, making it difficult for corrosive agents to reach the surface. The corrosive agents are faced with spatial hindrance (insufficient space to move within the coating, causing them to frequently change their path). The good corrosion resistance of the ZrN coating has also been proven in previous studies^{44,45}. The PN+DLC coating exhibited the lowest corrosion resistance among the coated samples. This behavior is related to the nature of the plasma-nitrided layer, which consists mainly of iron nitrides and expanded martensite formed by nitrogen diffusion into the substrate. Although this layer can enhance adhesion, its microstructure often contains columnar grains and microvoids, leading to a lower structural density compared to sputtered ZrN and TaN interlayers. During corrosion exposure, the nitrided layer tends to form an iron oxide film that is porous and loosely packed, facilitating the penetration of aggressive ions (e.g., Cl⁻) and promoting electrochemical reactions at the substrate surface. Furthermore, plasma nitriding may introduce microstructural inhomogeneities and residual stresses at the interface, which can act as preferential sites for localized corrosion initiation. In contrast, the denser, finer-grained, and more stable ZrN and TaN interlayers create a uniform and compact barrier that effectively impedes electrolyte penetration, thereby providing superior corrosion protection.

Conclusion

In this study, the effects of three different interlayers—plasma nitriding (PN), zirconium nitride (ZrN), and tantalum nitride (TaN)—on the structure, tribological behavior, and corrosion resistance of DLC coatings were investigated. The key findings are summarized as follows:

- Structural analysis using Raman spectroscopy revealed that the TaN+DLC sample exhibited the highest internal stress and sp³ content, indicating a more cross-linked and mechanically robust carbon structure. The lowest surface roughness was also observed in the TaN+DLC sample (3.31 nm), as measured by AFM, confirming a smooth and uniform surface morphology.
- Tribological tests showed that the TaN + DLC coating provided the lowest wear rate (0.001901 mm³/N·m) and
 the most stable friction behavior among all samples. This performance is attributed to the dense microstructure and enhanced interlayer adhesion confirmed by FESEM.
- Corrosion evaluation through EIS demonstrated that the TaN+DLC sample achieved the highest corrosion resistance, as evidenced by the largest Nyquist semicircle diameter and the highest charge transfer resistance. This superior electrochemical performance is attributed to the dense and stable TaN interlayer, which acts as an effective barrier against electrolyte penetration and reduces the likelihood of localized corrosion initiation.

Overall, the TaN interlayer significantly enhanced the structural, tribological, and corrosion properties of the DLC coatings compared to ZrN and PN. These findings suggest that TaN is a highly promising interlayer for applications requiring durable, wear-resistant, and corrosion-protective surfaces.

Data availability

The datasets generated during and/or analyzed during the current study are available from the corresponding author on reasonable request.

Received: 15 February 2025; Accepted: 9 September 2025

Published online: 13 October 2025

References

- 1. Adebowale, K. et al. Materials for cell surface engineering. Adv. Mater. 36, 2210059 (2024).
- 2. Liu, Z., Liu, X. & Ramakrishna, S. Surface engineering of biomaterials in orthopedic and dental implants: strategies to improve osteointegration, bacteriostatic and bactericidal activities. *Biotechnol. J.* 16, 2000116 (2021).
- 3. Khan, S. Å., Ferreira, F., Oliveira, J., Emami, N. & Ramalho, A. A comparative study in the tribological behaviour of different DLC coatings sliding against titanium alloys. *Wear* 554, 205468 (2024).
- 4. Evaristo, M., Fernandes, F. & Cavaleiro, A. Influence of the alloying elements on the tribological performance of DLC coatings in different sliding conditions. Wear 526, 204880 (2023).
- Zhao, Q., Kang, S., Zou, F. & Huo, Z. Structure and properties of Si and N co-doping on DLC film corrosion resistance. Ceram. Int. 49, 2121–2129 (2023).
- Shah, R. et al. DLC coatings in biomedical applications
 – Review on current advantages, existing challenges, and future directions.
 Surf. Coat. Technol. 131006 (2024). (2024).
- 7. Dhanola, A. Diamond-like Carbon (DLC) as a Biocompatible Coating for Biomedical Engineering, (2024).
- 8. Pougoum, F., Jedrzejczak, A., Azzi, M., Martinu, L. & Klemberg-Sapieha, J. E. Effect of interface roughness on the tribo-corrosion behavior of diamond-like carbon coatings on titanium alloy. *J Vac Sci. Technol. A* 40, (2022).
- Khan, S. A., Oliveira, J., Ferreira, F., Emami, N. & Ramalho, A. Surface roughness influence on tribological behavior of HiPIMS DLC coatings. *Tribol Trans.* 66, 565–575 (2023).
- 10. Piotrowska, K., Madej, M., Kowalczyk, J. & Radoń-Kobus, K. Surface roughness effects on the properties of silicon-doped diamond-like carbon coatings. *Coatings* 13, 1629 (2023).
- 11. Sharifahmadian, O., Pakseresht, A., Mosas, K. K. & Galusek, D. Doping effects on the tribological performance of diamond-like carbon coatings: A review. J. Mater. Res. Technol. 13, 2207–2221 (2023).
- 12. Wu, K. Y., Zhao, G. R., Li, Z. & Gong, Z. B. Effects of electrode distance on mechanical and tribological properties of hydrogenated DLC films deposited by DC-pulse PECVD. Surf. Rev. Lett. 28, 2050045 (2021).
- 13. Liu, Z. et al. Deposition of DLC film on the inner surface of N80 pipeline by Hollow cathode PECVD. Surf. Sci. Technol. 1, 12 (2023).
- Riley, P. R. et al. Enhanced vapor transmission barrier properties via silicon-incorporated diamond-like carbon coating. *Polymers* 13, 3543 (2021).
- 15. Lu, Y. et al. A review on diamond-like carbon films grown by pulsed laser deposition. Appl. Surf. Sci. 541, 148573 (2021).
- Shah, R. et al. DLC coatings in biomedical applications Review on current advantages, existing challenges, and future directions. Surf. Coat. Technol. 413, 131006 (2024).
- 17. Li, W. et al. Optimizing mechanical and tribological properties of DLC/Cr₃C₂-NiCr duplex coating via tailoring interlayer thickness. Surf. Coat. Technol. 434, 128198 (2022).
- 18. Zhao, Y. et al. Enhanced tribological and corrosion properties of dlc/crn multilayer films deposited by HPPMS. *Ceram. Int.* 48, 25569–25577 (2022).
- Wu, Y. et al. Design of Ta gradient layer to improve adhesion strength between Cu substrate and DLC film. Vacuum 203, 111221 (2022).
- 20. Kasiorowski, T. et al. Microstructural and tribological characterization of DLC coatings deposited by plasma enhanced techniques on steel substrates. Surf. Coat. Technol. 389, 125615 (2020).
- 21. Shioga, P. H. T., Binder, C., Hammes, G., Klein, A. N. & de Mello, J. D. B. Effects of different plasma nitrided layers on the tribological performance of DLC coatings. *Mater. Res.* 19, 1180–1188 (2016).
- 22. Singh, V., Sharma, R. K. & Sehgal, R. Impact of Deposition Pressure on the Structural, Nanomechanical, and Tribological Properties of δ-TaN Coatings Deposited Via Magnetron Sputtering on Ti6Al7Nb Alloy. P. I. MECH. ENG09544089241272870 (E-J PRO, 2024).
- Singh, V., Sharma, R. K., Sehgal, R. & Wani, M. F. The effect of RF sputtering power on structural, Nanomechanical and tribological properties of single layered TaN coatings. Surf. Topogr: Metrol. Prop. 12, 035003 (2024).
- 24. Farfan-Cabrera, L. I., Cao-Romero-Gallegos, J. A., Lee, S., Komurlu, M. U. & Erdemir, A. Tribological behavior of H-DLC and H-free DLC coatings on bearing materials under the influence of DC electric current discharges. *Wear* 522, 204709 (2023).
- 25. Tai, F. C., Lee, S. C., Chen, J., Wei, C. & Chang, S. H. Multipeak fitting analysis of Raman spectra on DLC-H film. J. Raman Spectrosc. 40, 1055–1059 (2009).
- 26. Kumar, I. & Khare, A. Raman spectra of PLD deposited DLC thin films on Si substrate. AIP Conf. Proc. 1591, 1018-1020 (2014).
- 27. Miki, Y., Nishimoto, A., Sone, T. & Araki, Y. Residual stress measurement in DLC films deposited by PBIID method using Raman microprobe spectroscopy. Surf. Coat. Technol. 283, 274–280 (2015).
- 28. Varade, A. et al. Detailed Raman study of DLC coating on Si (100) made by RF-PECVD. Procedia Eng. 97, 1452–1456 (2014).
- T FC, T. S. L. Correlation between I_D/I_G ratio from visible Raman spectra and sp²/sp³ ratio from XPS spectra of annealed hydrogenated DLC film. *Mater. Trans.* 47, 1847–1852 (2006).
- 30. Ferrari, A. C. & Robertson, J. Interpretation of Raman spectra of disordered and amorphous carbon. Phys. Rev. B. 61, 14095 (2000).
- 31. Robertson, J. Diamond-like amorphous carbon. Mater. Sci. Eng.: R: Rep. 37, 129-281 (2022).
- 32. Panda, M. et al. Nanoscale investigation of particulate contribution to diamond-like carbon film by pulsed laser deposition. RSC Adv. 6, 6016–6028 (2016).
- 33. Liu, G. et al. Optimizing the microstructure, mechanical, and tribological properties of Si-DLC coatings on NBR rubber for its potential applications. *Coatings* 10, 671 (2020).
- 34. Zhang, T. F. et al. Wear and corrosion properties of diamond-like carbon (DLC) coating on stainless steel, CoCrMo and Ti6Al4V substrates. Surf. Coat. Technol. 273, 12–19 (2015).
- 35. Kumar, I. & Khare, A. Raman spectra of PLD deposited DLC thin films on Si substrate. AIP Conf. Proc. 1591, 1018–1020 (2014).
- Wongpanya, P., Wongpinij, T., Photongkam, P. & Siritapetawee, J. Improvement in corrosion resistance of 316L stainless steel in simulated body fluid mixed with antiplatelet drugs by coating with Ti-doped DLC films for application in biomaterials. Corros. Sci. 208, 110611 (2022).
- 37. Tavakoli-Azar, T. et al. Synergistic effects of PVP-surface-treated CNTs and mg₂p₂o₇ nanoparticles on corrosion rate reduction of mild steel immersed in a 3.5% NaCl solution. *Inorg. Chem. Commun.* 174, 113848 (2025).

- 38. Davoodi, D., Emami, A. H., Vaghefi, S. M., Omidi, M. & Bakhsheshi-Rad, H. R. Deposition of electroless Ni-Cu-P coatings on L80 steel substrates and the effects of coatings thickness and heat treatment on the corrosion resistance. *Int. J. Press. Vessels Pip.* 200, 104823 (2022).
- 39. Zhang, Y., Gao, P., Chen, D. & Zhou, Y. Structure related corrosion behavior of DLC films in high cl⁻ environment. Corros. Rev. 39, 465–476 (2021).
- 40. Corona Gomez, J. Wear and corrosion resistance improvement of CoCrMo alloy by tantalum-based coatings. (Doctoral dissertation, University of Saskatchewan), (2022).
- 41. Rajak, D. K., Kumar, A., Behera, A. & Menezes, P. L. Diamond-like carbon (DLC) coatings: classification, properties, and applications. *Appl. Sci.* 11, 4445 (2021).
- 42. Babaei, K., Fattah-alhosseini, A., Elmkhah, H., Imantalab, O. & Ghomi, H. Studying the in vitro corrosion response of nanostructured TaN coatings in hank's physiological solution. *Int. J. Appl. Ceram. Technol.* 18, 1269–1280 (2021).
- 43. Singh, V., Sharma, R. K. & Sehgal, R. An experimental investigation on Nanomechanical and nanotribological behavior of tantalum nitride coating deposited on Ti6Al7Nb alloy. *Tribol Int.* **194**, 109461 (2024).
- 44. Mwema, F. M., Jen, T. C. & Zhu, L. Thin Film Coatings: Properties, Deposition, and Applications (CRC, 2022).
- 45. Chou, W. J., Yu, G. P. & Huang, J. H. Corrosion resistance of ZrN films on AISI 304 stainless steel substrate. Surf. Coat. Technol. 167, 59–67 (2003).

Acknowledgements

The authors thank Dr. Yazdan Shajari for his guidance during this research.

Author contributions

The authors confirm their contributions to the paper as follows: study conception and design: M.S.; data collection: M.J.E.; analysis and interpretation of results: M.S. and K.A. All authors reviewed the results and approved the final manuscript.

Funding

The authors did not receive support from any organization for the submitted work.

Declarations

Competing interests

The authors declare no competing interests.

Declaration of competing interest

The authors declare that they have no known competing financial interests or personal relationships that could have appeared to influence the work reported in this paper.

Additional information

Correspondence and requests for materials should be addressed to M.J.E.

Reprints and permissions information is available at www.nature.com/reprints.

Publisher's note Springer Nature remains neutral with regard to jurisdictional claims in published maps and institutional affiliations.

Open Access This article is licensed under a Creative Commons Attribution-NonCommercial-NoDerivatives 4.0 International License, which permits any non-commercial use, sharing, distribution and reproduction in any medium or format, as long as you give appropriate credit to the original author(s) and the source, provide a link to the Creative Commons licence, and indicate if you modified the licensed material. You do not have permission under this licence to share adapted material derived from this article or parts of it. The images or other third party material in this article are included in the article's Creative Commons licence, unless indicated otherwise in a credit line to the material. If material is not included in the article's Creative Commons licence and your intended use is not permitted by statutory regulation or exceeds the permitted use, you will need to obtain permission directly from the copyright holder. To view a copy of this licence, visit https://creativecommons.org/licenses/by-nc-nd/4.0/.

© The Author(s) 2025